Radiative and Nonlinear Influences on Orographic Gravity Wave Drag

MICHAEL J. WEISSBLUTH AND WILLIAM R. COTTON

Department of Atmospheric Science, Colorado State University, Fort Collins, Colorado

(Manuscript received 19 September 1988, in final form 22 May 1989)

ABSTRACT

Vertical divergence of the mountain wave's momentum flux has recently been hypothesized to be an important contribution to the global momentum budget. Wavebreaking theories and envelope orography have been employed to explain the divergence of the momentum flux. Here, cloud-top radiational cooling is shown to locally destabilize the environment and disrupt the propagation of the mountain wave in idealized two-dimensional simulations, thus drastically altering the expected momentum flux profile. Also, simulations of two-dimensional mountain waves indicate that nonlinearities can increase the wave response if the lower layer is decoupled from the flow aloft or decrease the wave response by providing multiple reflection levels for the incident mountain wave. The onset of wavebreaking and the level at which the wave breaks can be influenced by the ambient thermodynamic profile.

1. Introduction

Gravity waves have long been known to play important roles in atmospheric processes occurring over a broad range of space and time scales. In large eddy simulations (LESs) and mesoscale models, gravity waves have been for the most part explicitly modeled since the grid spacing has been small enough to capture the forcing and response of the atmosphere. In particular, mesoscale models have been successfully used to simulate the mountain waves produced when there is flow over topography (e.g., Durran and Klemp 1983). Durran and Klemp (1983) also examined the behavior of mountain waves in the presence of moisture and found that there is a small change in the vertical wavelength and amplitude of the mountain wave due to the slight decrease in the Brunt–Väisäla frequency.

General circulation models (GCMs), however, are inherently unable to explicitly simulate orographic gravity waves due to their present grid spacing. The inability of GCMs to resolve this important class of waves can be conceptualized by considering the atmosphere's response to stratified flow over idealized topography as in Emanuel (1986). Two regimes of oscillatory flow are possible; the first is when the wavelength of the topography lies between $2\pi U/N$ and $2\pi U/f$ (inertia–gravity waves) and the second is when the wavelength of the topography is greater than $2\pi\sqrt{U/\beta}$ (planetary-scale Rossby waves). Here U is the constant zonal wind speed flowing over the topography, f is the Coriolis parameter N is the Brunt-Väisäla frequency and β is the meridional change of f. This implies that the grid spacing needed to minimally resolve the longest gravity wave wavelength is 150 km using $U = 10$ m s^{-1} and $f = 10^{-4}$ s^{-1}. GCMs may be approaching this now, but obviously there will always be a significant amount of gravity wave energy that may never be captured by these models.

Recently, the inability of the GCM to capture the mountain wave has been hypothesized to cause systematic biases in the model fields (Slingo and Pearson 1986). Correct estimates of the Southern Hemisphere's wind fields in the summer and winter and Northern Hemisphere's wind fields in the summer lend credibility to the model physics, but the Northern Hemisphere's wind fields are systematically overestimated in the winter. The problem, then, may be linked to the strong winter flow over mountain ranges (which are relatively sparse in the Southern Hemisphere). Therefore, two mechanisms have been proposed to induce drag in the Northern Hemisphere's winter westerlies. Envelope orography (Wallace et al. 1983) reduced systematic errors in the European Centre for Medium-Range Weather Forecasting's GCM by enhancing the land surface elevations preferentially over major mountain ranges. This reduced the westerly momentum through pressure torques exerted on the mountain by the prevailing westerly current. Unfortunately, systematic errors then appeared in the Northern Hemisphere's summer due to unrealistic elevated heating.

Another approach used more successfully was the introduction of a gravity wave drag parameterization proposed by Palmer et al. (1986). The basis for this scheme is as follows. Flow over topography produces mountain waves which, in the absence of transience or dissipation, create a stress profile independent of

Corresponding author address: Dr. W. R. Cotton, Department of Atmospheric Science, Colorado State University, Fort Collins, CO 80523.

height (Eliassen and Palm 1961). Because only the vertical divergence of the stress profile affects the mean momentum equations, gravity waves might be expected to have little impact on GCM simulations; however, wave breaking is hypothesized to create the required divergence in the stress profile to decelerate the westerly flow. Palmer et al. (1986) based their parameterization on linear theory to calculate a surface stress and distribute this stress vertically with a wave-dependent Richardson number. Wave breaking and momentum absorption occurred preferentially in the planetary boundary layer (PBL) and the lower stratosphere. These are precisely the places where Slingo and Pearson (1986) found the largest model biases in predicted wind fields.

Other sources of gravity waves have been proposed to affect the mean momentum equations. Rind et al. (1988) included parameterizations of shear-generated gravity waves and convectively generated gravity waves in their global model. Flux divergences were assumed to occur through a wavebreaking mechanism, as above. Because their concern centered on the middle atmosphere, however, they did not consider the flux divergence of gravity waves below the middle troposphere. Orographic gravity waves were found to break in the lower stratosphere, consistent with Palmer et al. (1986). Shear and convectively generated gravity waves, on the other hand, were found to break in the mesosphere since their parameterized amplitudes were several magnitudes lower than the terrain generated gravity waves.

In a recent numerical simulation of the genesis of mesoscale convective systems (MCSs) over the Colorado mountains, Tripoli and Cotton (1989a,b) found that longwave radiational cooling at the tops of the stratiform-anvil clouds of MCSs induces an unstable layer that inhibits the vertical propagation of gravity wave energy emitted by the deep convective clouds. The resultant trapped gravity waves interfere with the emitted gravity waves thereby altering the convective structure and evolution of the simulated MCS. Motivated by these results, we hypothesize that gravity waves triggered by stably stratified flow over mountain barriers can also become trapped by radiative cooling when clouds are present and thereby alter the mountain wave's momentum flux. Because major orographic barriers such as the Rocky Mountains are frequently covered by cap clouds or shrouded by blanket clouds in the winter months, we hypothesize that trapping of gravity waves can lead to systematic changes in mountain wave momentum fluxes and biases in gravity wave drag parameterization schemes.

To examine this hypothesis, idealized two-dimensional simulations of stably stratified flow over a mountain barrier with and without cloud-top radiative effects are performed. In the following sections, the two-dimensional model will be briefly described. Then, several idealized experiments will be presented that indicate the importance of radiative cooling in altering momentum flux profiles. Specifically, the momentum flux profiles are examined when there is flow over 100 m, 500 m and 1000 m mountains in the control experiments. The effects of moisture are then examined in altering these control wave stress profiles. Longwave radiational cooling and warming will then be added and found to profoundly influence the propagation of the mountain wave. Finally, the nonlinear effects which modify the wave stress profile are examined in two atmospheres which have different stability profiles.

2. Overview

The response of the atmosphere to flow over topography is well known and the reader is referred to Smith (1979) for a comprehensive review. The vertical wavelength of the mountain wave, λ, is characterized by the Scorer parameter l, (Scorer 1949). Neglecting the effects of compressibility,

$$l^2 = \frac{N^2}{U^2} - \frac{1}{U}\frac{\partial^2 U}{\partial z^2}$$

where N and U are as before. When l changes slowly with height relative to λ, the familiar WKB approximation is adequate to describe the behavior of the mountain wave. When l changes rapidly, however, partial or total reflection of wave energy is possible.

Blumen (1965) and Klemp and Lilly (1975) have shown that the gravity wave will be reflected with a phase reversal when encountering a region where l increases rapidly with height and will be reflected without a phase reversal when l decreases with height. Therefore, the wave response will be maximized beneath the reflecting layer when the distance between the reflecting layer and the ground is an integral multiple of $\frac{1}{2}\lambda$ in the increasing l case, and an odd integral multiple of $\frac{1}{4}\lambda$ in the decreasing l case.

The inverse Froude number, $\mathrm{Fr}^{-1} = Nh/U$, is useful for characterizing the nonlinearity and the blocking potential for the flow. If $\mathrm{Fr}^{-1} \ll 1$, then the flow is linear and if $\mathrm{Fr}^{-1} > 0.85$ in an atmosphere with constant density, the nonlinearities become strong enough to force overturning streamlines and consequent wavebreaking. The critical value which separates the laminar flow without wavebreaking and the turbulent flow with wavebreaking varies considerably in the following experiments. In this paper, weak wavebreaking refers to flows having Fr^{-1} near this critical value, while strong wavebreaking refers to flows having Fr^{-1} significantly greater than this threshold value. The flow is also blocked and local flow reversal upstream of the mountain occurs when $\mathrm{Fr}^{-1} > 0.85$. In our experiments, the nonlinearities in the flow become significant when $\mathrm{Fr}^{-1} \sim 0.2$.

3. Experimental design

In order to numerically investigate the behavior of the mountain wave and its associated momentum flux,

the Colorado State University RAMS (Regional Atmospheric Modeling System) is used in the form reported in Tripoli and Cotton (1982, 1989a,b). Options include the nonhydrostatic primitive equations expressed in a terrain following coordinate system, condensation of water vapor (but without precipitation or the ice phase) and the longwave radiation parameterization developed by Chen and Cotton (1983). A Klemp–Wilhelmson lateral radiative boundary condition with a mesoscale compensation region (MCR, Tripoli and Cotton 1982) is used. The upper boundary condition is the Klemp–Durran radiative boundary condition (Klemp and Durran 1983). A constant grid spacing of 2 km in the horizontal and 250 m in the vertical is used creating a domain 160 km long and 8 km high. Terrain is specified by the bell-shaped mountain

$$z_s = \frac{ha^2}{x^2 + a^2}$$

with various heights h and a half-width a of 10 km. The model is initialized with a horizontally homogeneous base state.

Initializing the model with moisture requires some discussion. In particular, the base state is initialized with all of the water as vapor. If the base state is supersaturated, cloud water is diagnosed during the first time step and the resultant condensation heats the supersaturated layers, causing a discontinuity in the temperature. Since, in later sections, we are interested in the effects of moisture on the propagation of the mountain wave, the discontinuity in temperature after the cloud water is diagnosed is not desirable since it may lead to wave reflection. Therefore, the base state with moisture is altered so that after condensation, the temperature will be more continuous at cloud top. While an iterative procedure might be needed to provide a strictly continuous temperature profile at cloud top, in view of the complicating effects of cloud water on the moist Brunt–Väisäla frequency, we simply reduced the base state temperature by the amount of heating which would have been produced by condensation at the desired base state temperature. The resultant temperature profile is judged in a later section to produce an adequately smooth profile of the Scorer parameter.

The experiments performed are summarized in Table 1. Moisture and radiation effects are investigated in the first main group of experiments and nonlinear effects are investigated in the second main group of experiments. CONTROL 0 is performed to gauge the model's accuracy in reproducing a linear hydrostatic mountain wave. In anticipation of the results of experimental group C, the rest of the experiments are run with λ halved (by halving U) so that the mountain wave will be sensitive to vertical changes in the thermodynamic profile. The remainder of the control group and experimental groups A and B are run with 100 m, 500 m and 1000 m mountains which produce weak, moderate and strong nonlinear effects, respectively. Experimental groups A and B are initialized with cloud water but group B includes longwave radiational warming and cooling.

TABLE 1. Summary of the experiments. PROFILE indicates the initial thermodynamic profile of the experiment. Here N_i represents the stability of an isothermal atmosphere at 273 K; "1" represents an atmosphere with stability N_i except for a thin mixed layer at $1/4\lambda$ as delineated in Fig. 14c; "2" represents a three-layer atmosphere with a middle mixed layer and a lower layer of stability N_i and an upper layer of stability $2N_i$ as delineated in Fig. 15c.

Expt.	h (m)	U (m/s)	Fr^{-1}	Moist	Rad	Profile
CONTROL 0	10	15.	0.0094	No	No	$3/4N_i$
CONTROL 1	100	7.5	0.19	No	No	$3/4N_i$
CONTROL 2	500	7.5	0.94	No	No	$3/4N_i$
CONTROL 3	1000	7.5	1.9	No	No	$3/4N_i$
A1	100	7.5	0.19	Yes	No	$3/4N_i$
A2	500	7.5	0.94	Yes	No	$3/4N_i$
A3	1000	7.5	1.9	Yes	No	$3/4N_i$
B0	—	7.5	—	Yes	Yes	$3/4N_i$
B1	100	7.5	0.19	Yes	Yes	$3/4N_i$
B2	500	7.5	0.94	Yes	Yes	$3/4N_i$
B3	1000	7.5	1.9	Yes	Yes	$3/4N_i$
C0	10	20	0.0094	No	No	1
C1	10	10	0.019	No	No	1
C2	10	10	0.019	No	No	2
D1	100	10	0.19	No	No	1
D2	100	10	0.19	No	No	2
E1	500	10	0.94	No	No	1
E2	500	10	0.94	No	No	2
F1	1000	10	1.9	No	No	1
F2	1000	10	1.9	No	No	2

The second main group investigates nonlinear effects with two thermodynamic profiles representative of a thin mixed layer in an otherwise isothermal atmosphere and a three-layer atmosphere. Experimental groups C, D, E and F examine the two thermodynamic profiles with 10 m, 100 m, 500 m and 1000 m mountains, respectively. Experiment C0 helps show that the depth of the mixed layer must be large compared to λ to influence the propagation of the mountain wave. The results of these nonlinear experiments are summarized in graphical form at the end of the section.

4. Results and discussion

In the following subsections, we first examine the wave stress profile produced by flow over 10 m, 100 m, 500 m and 1000 m mountains. The modifying effects of moisture on these control profiles are then examined. Longwave radiational warming and cooling is then introduced to examine how the modified thermodynamic profile influences the propagation of the mountain wave. Finally, nonlinear effects are quantified in two atmospheres having a three-layer structure.

The various experimental results are shown in groups

of three figures; the first is the vertical motion field from X = −80 km to X = 80 km (which excludes the MCR) and the second and third are vertical profiles of the normalized horizontal momentum flux and Scorer parameter averaged over the right half of the domain, respectively. When static stabilities are needed, as in the calculation of Scorer parameter, a moist Brunt–Väisäla frequency is used (Durran and Klemp 1982). In the second main experimental group which investigates nonlinear effects, the perturbation streamfunction is included as a fourth figure. The wave stress is normalized to its linear hydrostatic value and is shown at the four nondimensional times indicated on the figure. Nondimensional times are given by $T = Ut/a$, where t is the dimensional time and a is the mountain half-width.

a. Control runs

We examine the wave momentum flux for flow over 10 m, 100 m, 500 m and 1000 m mountains in the following control runs. The results from flow over the 10 m mountain will verify the model physics. The remaining three control experiments are used as a base to help quantify the effects of moisture and long wave radiational warming and cooling on the wave momentum flux profile produced in the experiments in the following subsections.

The CONTROL 0 run shown in Fig. 1 typifies the hydrostatic linear mountain wave solution for a 10 m mountain. The momentum flux reaches about 93% of the analytic value at a height of 7 km which is near one vertical wavelength at $T = 59$. This can be considered the practical limit on the model's flux computation and provides a base to judge the following experiments. It is important to note that the flux does approach a constant value with height in accordance with the Eliassen–Palm theorem mentioned earlier.

In CONTROL 1, the mountain height is raised to 100 m and the zonal wind is halved, thus halving the vertical wavelength. In CONTROL 1, $Fr^{-1} = 0.19$ and the flow is expected to be slightly nonlinear; evidence of this can be seen in both the normalized momentum flux (Fig. 2b) and the averaged Scorer parameter (Fig. 2c) as oscillations in the vertical profiles.

The mountain height is raised to 500 m in CONTROL 2. In this case, $Fr^{-1} = 0.94$ and wavebreaking is evident in Fig. 3c where locally large values of the Scorer parmameter occur. Large values should be expected since overturning streamlines imply local flow reversal and thus minima in the wind speed of the disturbed flow. The efficiency of the breaking wave in trapping the momentum flux of the gravity wave is evident in Fig. 3b, where the momentum flux near the ground is three times larger than its linear hydrostatic value. Clark and Peltier (1984) also found similar momentum fluxes under breaking waves and concluded that this amplification was due to a resonance phenomenon produced when the incident wave was reflected from the region of wavebreaking.

Strong wavebreaking occurs in CONTROL 3 for the strongly nonlinear flow over the 1000 m mountain (Fig. 4). The wavebreaking begins very early in this simulation and is efficient is producing high surface momentum fluxes. These four control experiments indicate the potential importance that wavebreaking might have in causing large flux divergences in orographic mountain waves.

b. Moisture effects

The following three experiments add moisture to the control simulations of flow over 100 m, 500 m and

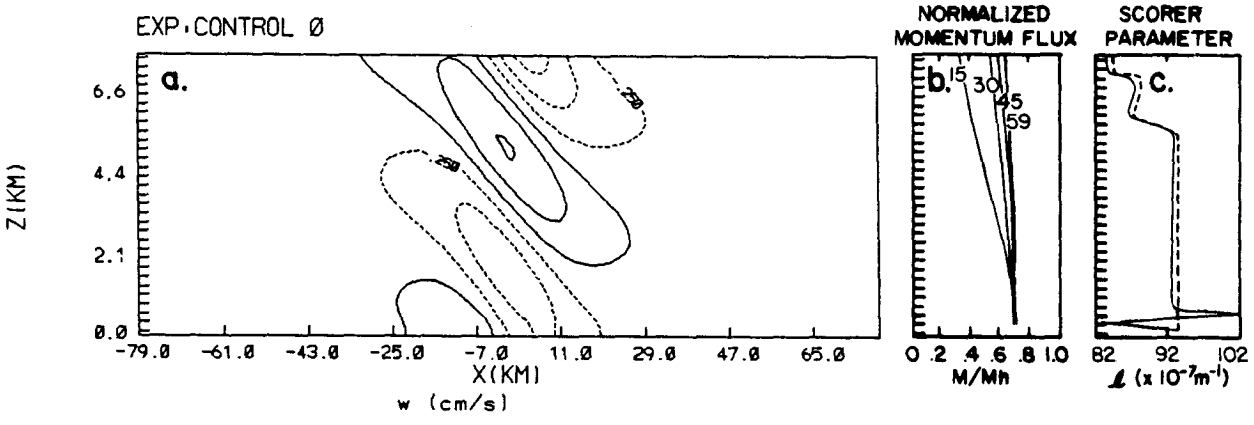

FIG. 1. Representation of the vertical motion field in cm s^{-1} after 8 hours of the simulation for CONTROL 0 which simulates flow over a 10 m mountain. Solid lines indicate upward motion while dashed lines indicate downward motion. Contours are every 0.5 cm s^{-1}. Shown to the right in panel (b) is a vertical profile of the momentum flux. The values are normalized to their linear hydrostatic analytic value. A vertical profile of the Scorer parameter at 8 hours averaged over the eastern half of the domain is shown in panel (c). The dotted line indicates the initial Scorer parameter profile and is equivalent to the initial stability if multiplied by the zonal wind indicated in Table 1 of the text.

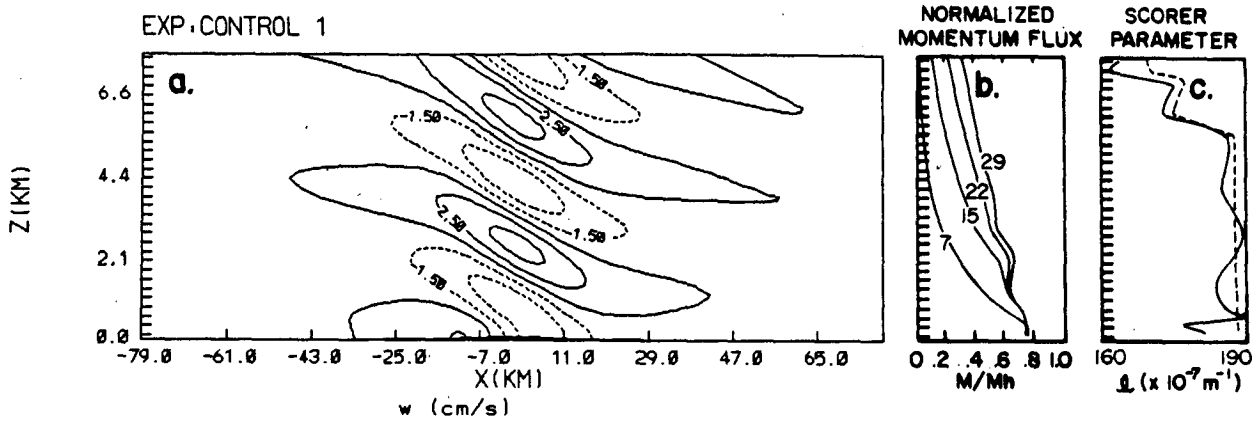

FIG. 2. Similar to Fig. 1 except for CONTROL 1 which simulates flow over a 100 m mountain. Contours are every 0.5 cm s^{-1}.

1000 m mountains (CONTROL 1–CONTROL 3) in order to isolate the radiational effects investigated in the following subsection. The experiments were initialized with a relative humidity of 150% (corresponding to a liquid water equivalent of about 3 g kg^{-1} at a height of 2 km in an isothermal atmosphere at 273 K) so that the lee-side subsidence and the associated drying would evaporate all of the water only in the 1000 m mountain run. Although this initially creates an extreme moisture gradient (3 g kg^{-1} in 250 m), turbulent processes quickly operate to produce a more realistic vertical profile of moisture (3 g kg^{-1} in 1 km) in the 500 m mountain run by 4 hours. Wesley and Pielke (1988) documented a wintertime storm along the east slope of the Rocky Mountains that indicates the existence of large moisture gradients near cloud top. They found gradients in moisture, not including cloud water, of 1 g kg^{-1} in 1 km so that the 3 g kg^{-1} in 1 km moisture gradient used here seems plausible.

Initializing the atmosphere with cloud water and obtaining a constant Scorer parameter is difficult due to the dependence of N on cloud water (Durran and Klemp 1982) and the particular way this model is initialized as discussed in the experimental design section. The initial profile as shown by the dotted line in Fig. 5c is a compromise between having a relatively smooth Scorer parmameter with height and having enough cloud water to sustain a cloud in spite of the lee-side drying in the wave subsidence regime.

Experiment A1 shows the moisture effects on a 100 m mountain wave. The momentum flux in Fig. 5b diverges when $T = 7$ as the wave encounters the level where the Scorer parameter changes abruptly (Fig. 5c). The flux does, however, eventually reach a fairly steady value at later nondimensional times, indicating that the initialization procedure is satisfactory. Because moisture reduces N by about 25%, the momentum flux is reduced by a commensurate amount, as seen by comparing Fig. 5b to Fig. 2b. Moisture, in this case, mainly damps the wave amplitude.

The addition of moisture can also inhibit wavebreaking by reducing the wave's momentum flux, as in Expt. A2 (Fig. 6). This can have important implications in GCMs since the regions where wavebreaking

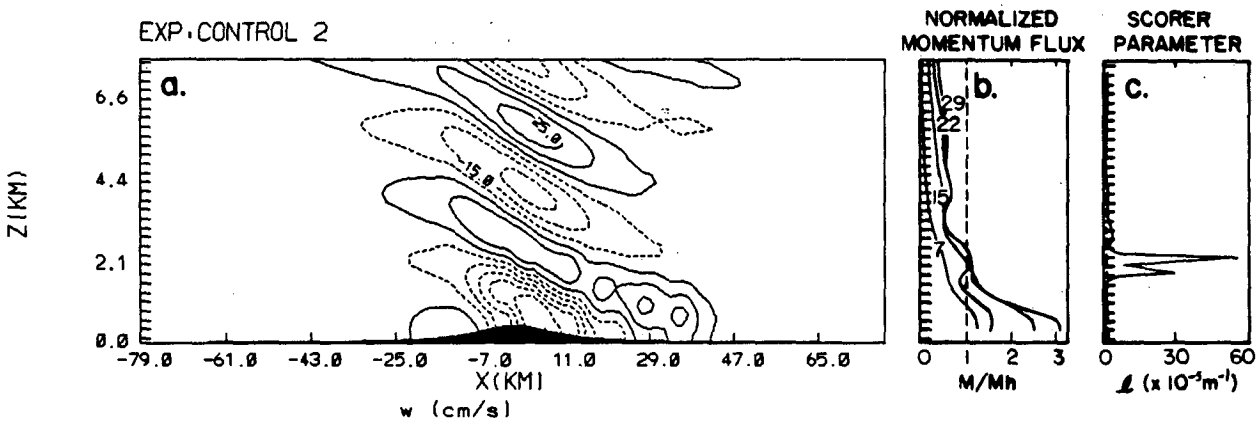

FIG. 3. Similar to Fig. 1 except for CONTROL 2 which simulates flow over a 500 m mountain. Contours are every 10 cm s^{-1}.

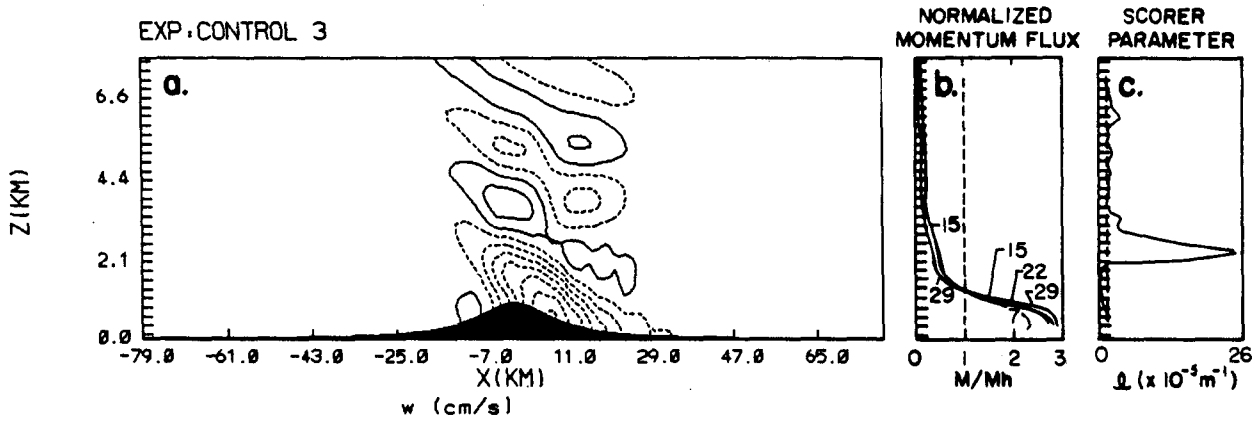

FIG. 4. Similar to Fig. 1 except for CONTROL 3 which simulates flow over a 1000 m mountain. Contours are every 20 cm s^{-1}.

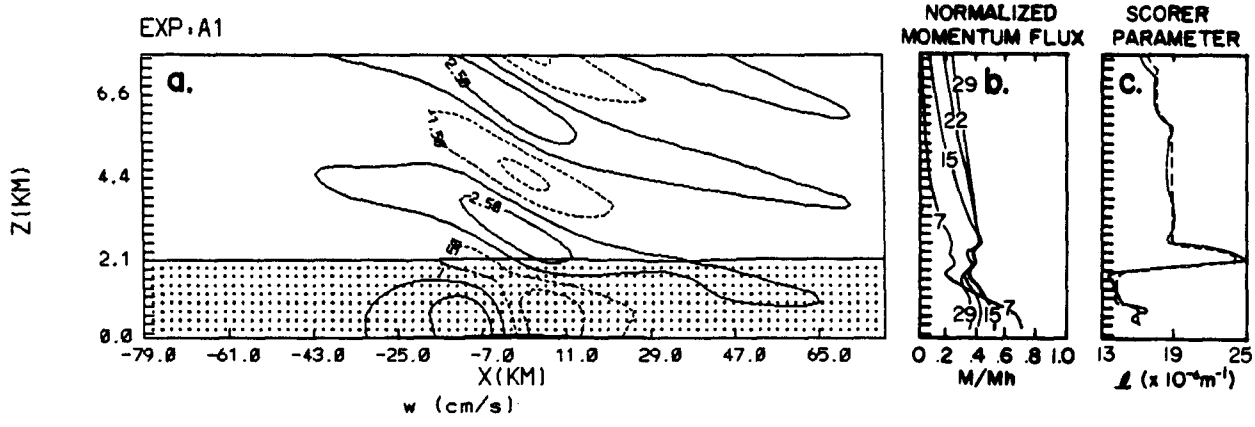

FIG. 5. Similar to Fig. 1 except that the model is initialized with 150% relative humidity in the lowest 2 km for Expt. A1, which simulates flow over a 100 m mountain. Contours are every 2 cm s^{-1}.

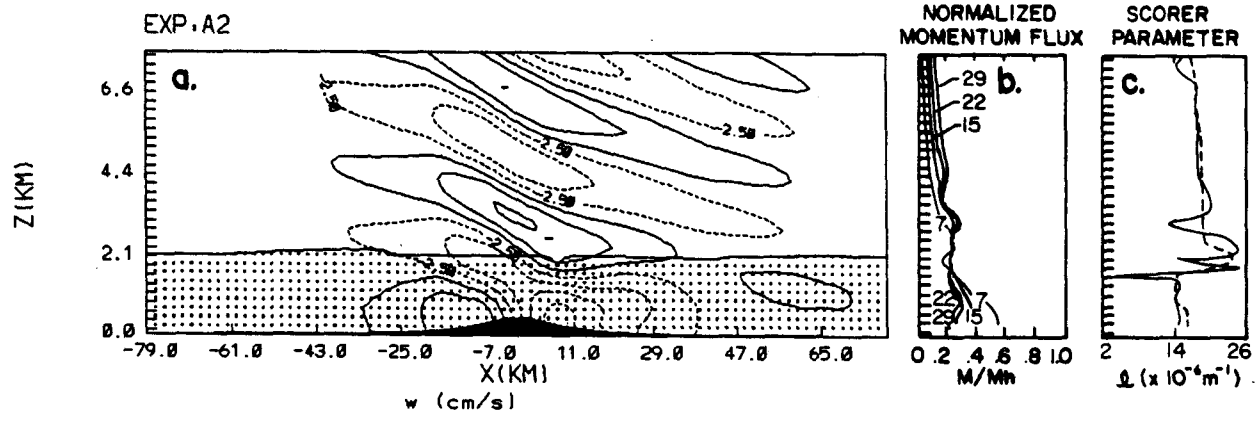

FIG. 6. Similar to Fig. 5 except for Expt. A2, which simulates flow over a 500 m mountain. Contours are every 5 cm s^{-1}.

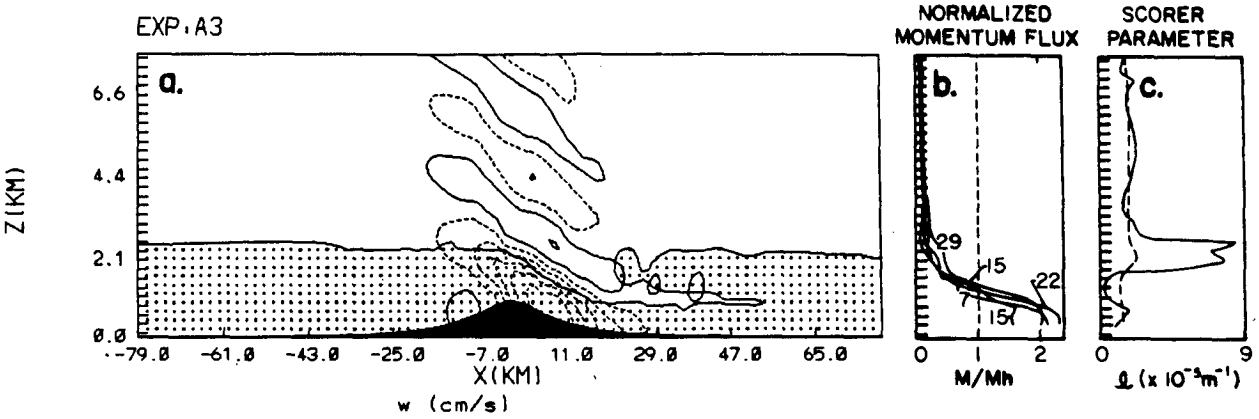

FIG. 7. Similar to Fig. 5 except for Expt. A3, which simulates flow over a 1000 m mountain. Contours are every 20 cm s^{-1}.

might be expected to occur and produce large divergences of the wave stress might, in fact, be regions where no divergence of the momentum flux occurs.

In Expt. A3, the lee-side subsidence is strong enough to evaporate some of the initialized cloud water. The wave then breaks in accordance with Froude number arguments. The surface momentum flux in Fig. 7b is only twice the hydrostatic value and about 75% of the value when moisture is not present (compare to Fig. 4b).

Therefore moisture will damp the mountain wave whether or not wavebreaking occurs. Moisture will also inhibit the formation of wavebreaking, thus increasing the threshold inverse Froude number which determines when wavebreaking should occur.

c. *Radiation effects*

Since radiational cooling at cloud top may significantly change the stability profile, the addition of a longwave radiation scheme may produce significant differences in the nature of the mountain wave and the resultant momentum flux profiles. The following experimental group B is initialized with 150% relative humidity as in group A but includes longwave radiational cooling and warming in 100 m, 500 m and 1000 m mountain runs. The initial moisture gradient is extreme and forces strong radiational cooling at cloud top but by 4 hours, the moisture and temperature profiles are realistic, as discussed in the previous section. Experiment B0 indicates the atmospheric response with no topography while Expts. B1–B3 can be compared to Expts. A1–A3.

Experiment B0 (Fig. 8) shows that cloud top radiational cooling destabilizes the cloud layer until conditional instability develops. Longwave radiational cooling first destabilizes the atmosphere just below cloud top since the radiative flux divergence is largest there. This forces N and thus l towards zero which can be seen in Fig. 8b near two kilometers.

In Expt. B1, a 100 m mountain is introduced and the resultant fields are shown in Fig. 9. As was hypothesized, the abrupt decrease in the Scorer parameter partially traps the mountain wave energy. This trapped

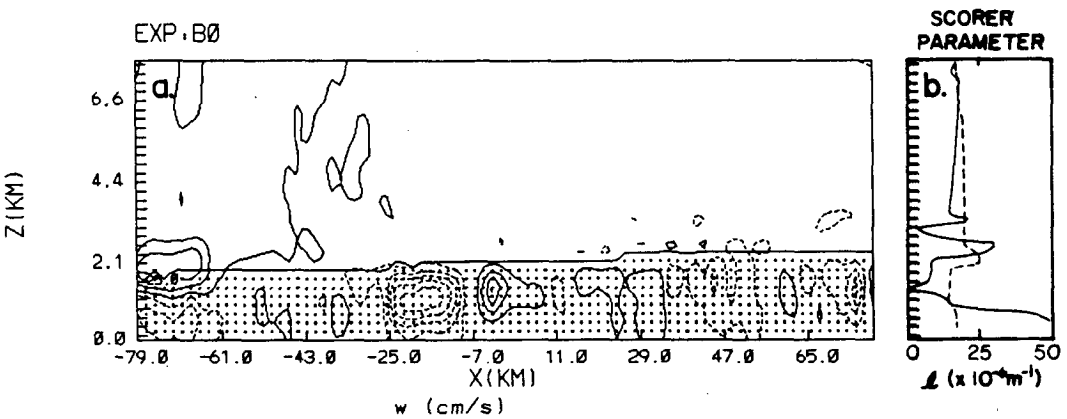

FIG. 8. Similar to Fig. 5 except for Expt. B0, which simulates flow with no topography. Longwave radiational cooling and warming are allowed. Contours are every 10 cm s^{-1}.

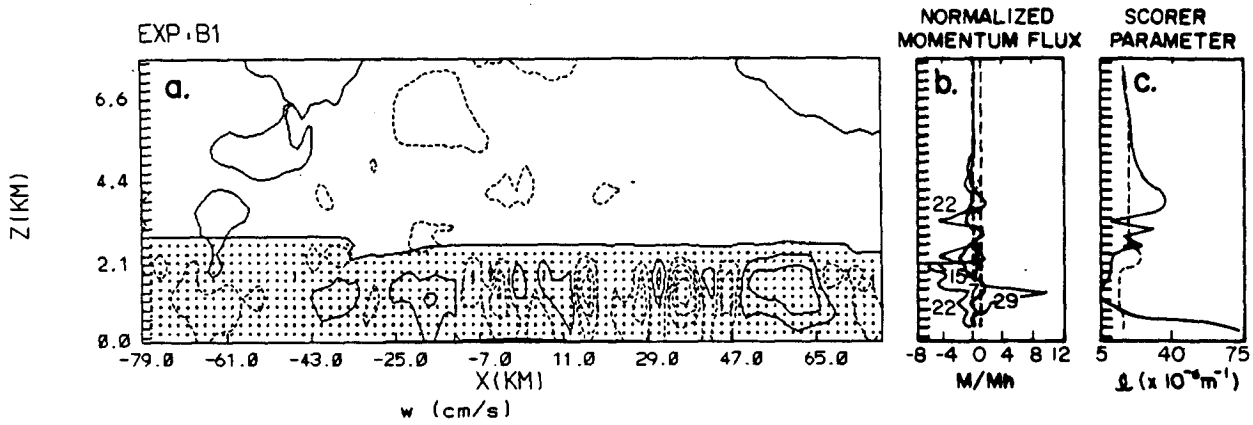

FIG. 9. Similar to Fig. 8 except for Expt. B1, which simulates flow over a 100 m mountain. Contours are every 10 cm s^{-1}.

energy then forces vertical motions within the now conditionally unstable cloud layer. This process is efficient in triggering conditional convective instability since the convection is initiated several hours before the convection in Expt. B0, but there do not appear to be any significant differences in the nature of the convection. The momentum fluxes produced by the convection are up to an order of magnitude larger than the momentum flux obtained from a 100 m mountain in CONTROL 1 and A1. These small scale convective motions have disrupted the propagation of the mountain wave; indeed the vertical motion field (Fig. 9a) indicates the absence of any recognizable mountain wave pattern.

The fields for a 500 m mountain and 1000 m mountain are shown in Figs. 10 and 11, respectively. The convective momentum fluxes are several times weaker than the momentum fluxes for these mountains. The vertical motion field for the 1000 m mountain (Fig. 11a) shows that due to the increased amplitude of the mountain wave, some of the energy has propagated through the cloud layer; the momentum flux profile (Fig. 11b), however, shows that this transmitted energy is less than 10% of the hydrostatic value. It is also interesting that the radiational cooling has offset the lee-side drying effects that evaporated the cloud in Expt. A3.

While experimental group A shows that moisture can decrease the momentum flux by 25% and inhibit wavebreaking, experimental group B shows that cloud-top radiational cooling has a profound affect on the propagation of the mountain wave. The small-scale convective motions which develop in the conditionally unstable cloud efficiently disrupt the propagation of the mountain wave and eliminate or significantly reduce any associated momentum flux. Analysis of the experimental group B indicate only small quantitative differences between the convection which develops within the destabilized layer for the three mountain heights.

d. Nonlinear effects

In order to investigate the nonlinear effects on the propagation of the mountain wave, a three-layer atmosphere is chosen as shown in Fig. 12c. This simple model was chosen because analytic solutions exist and

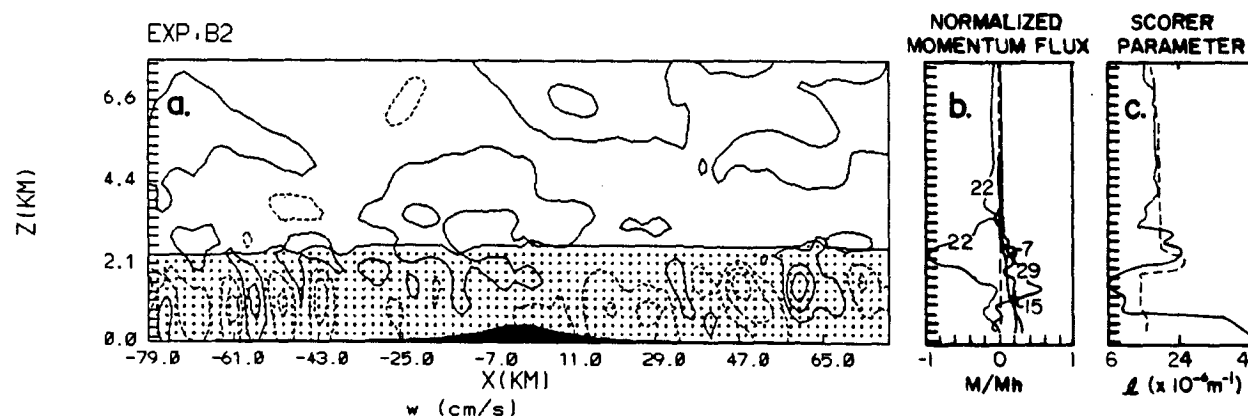

FIG. 10. Similar to Fig. 8 except for Expt. B2, which simulates flow over a 500 m mountain. Contours are every 10 cm s^{-1}.

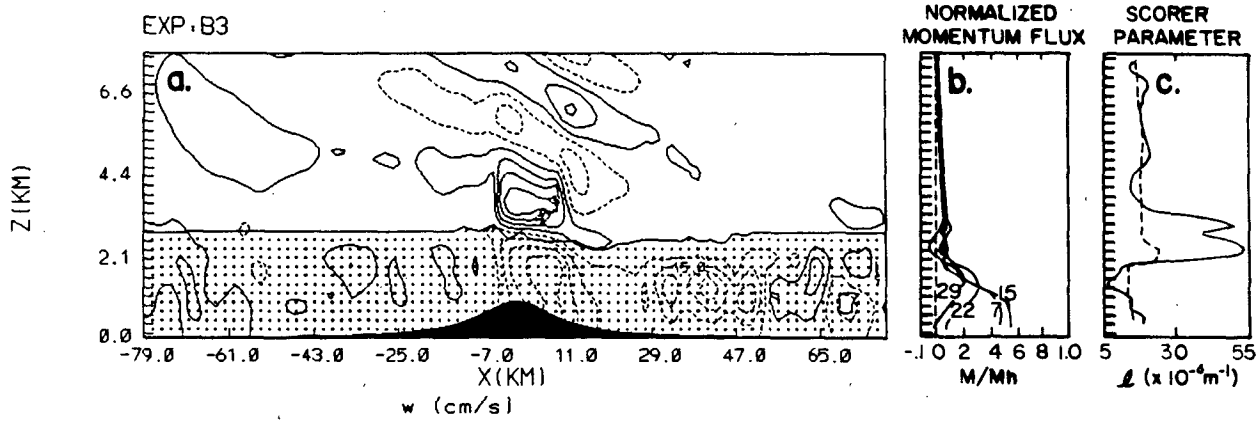

FIG. 11. Similar to Fig. 8 except for Expt. B3, which simulates flow over a 1000 m mountain. Contours are every 10 cm s^{-1}.

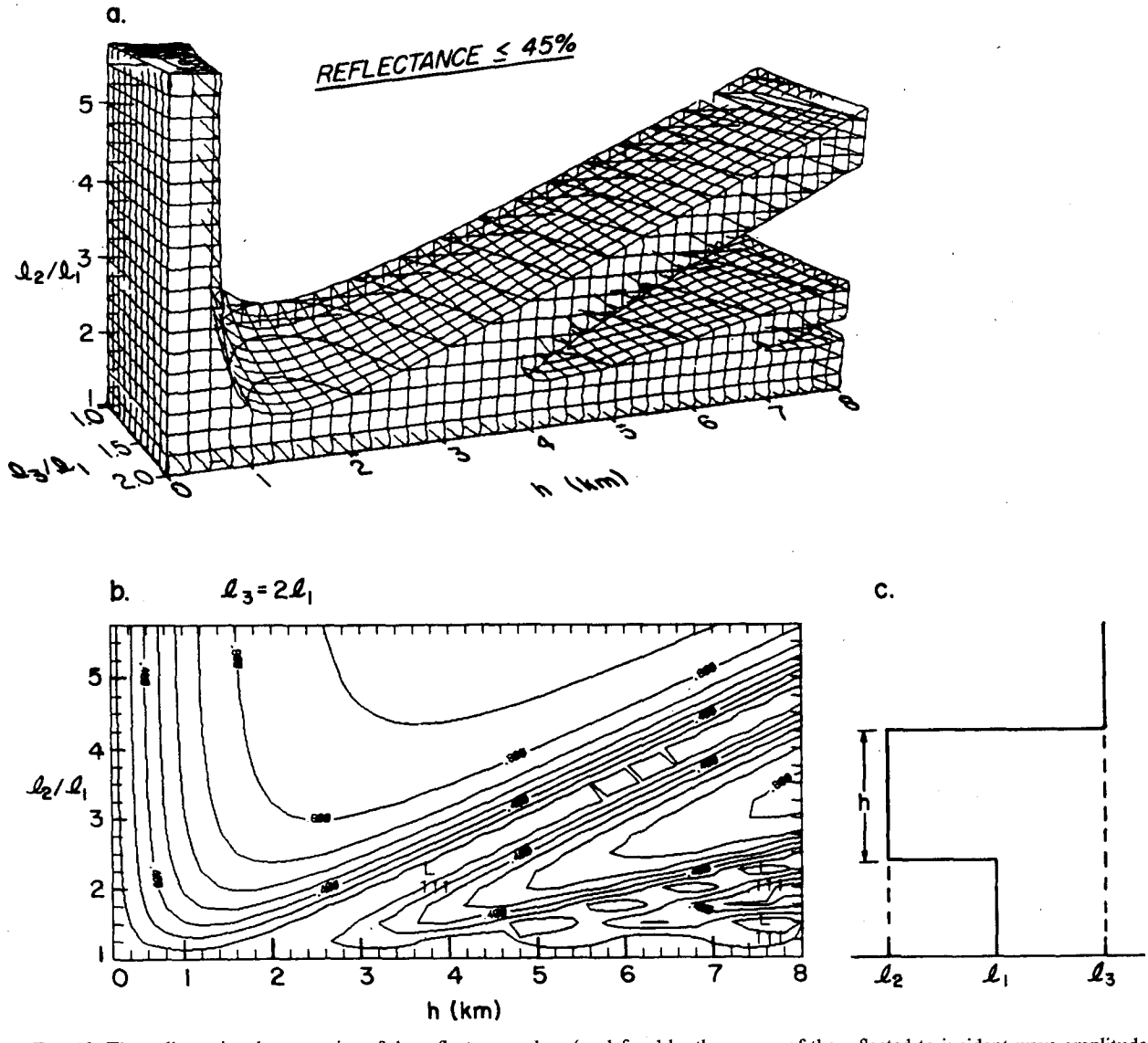

FIG. 12. Three-dimensional perspective of the reflectance values (as defined by the square of the reflected to incident wave amplitude) less than 45% are plotted in panel (a) for the three-layer atmosphere indicated in panel (c). A two-dimensional slab at $l_3 = 2l_1$ is shown as a point of reference in panel (b).

the stability profile of a radiationally cooled cloud layer exhibits three distinct layers. This three layer structure could also be produced by processes such as differential temperature advection, surface energy fluxes or large-scale lifting.

Allowing for reflection from the first two layers and applying a radiation upper boundary condition, Eliassen and Palm (1961) derived the following linear formula for the ratio r of the square of the reflected to incident wave in the lowest layer:

$$r = \frac{\lambda_2^2(\lambda_1 - \lambda_2)^2 - (\lambda_2^2 - \lambda_1^2)(\lambda_3^2 - \lambda_2^2)\sin^2\lambda_2 h}{\lambda_2^2(\lambda_1 + \lambda_2)^2 - (\lambda_2^2 - \lambda_1^2)(\lambda_3^2 - \lambda_2^2)\sin^2\lambda_2 h}$$

where λ_1, λ_2 and λ_3 are the wavenumbers of the wave in the lower, middle and upper layers, respectively. Assuming hydrostatic balance, the solution to the above equation is plotted for all $r < 0.45$ in Fig. 12a for the range of parameters $1 < l_3/l_1 < 2$, $1 < l_2/l_1 < 6$ and $h < 8000$ m. A two-dimensional slab at $l_3/l_1 = 2$ is shown as a point of reference in Fig. 12b. As the depth of the middle layer increases, the solutions become more oscillatory as discussed in Eliassen and Palm (1961). Using a three-dimensional perspective, system behavior can be charted by following lines of constant reflectivity. For example, beginning at $h \sim 1$ km and $l_2/l_1 = 2$, one can see that as the depth of the interface increases, smaller values of l_3/l_1 are needed to maintain the same reflectance until $h \sim 1.5$ km where larger values are then needed. Also, as l_3/l_1 decreases, the maximum response is obtained with increasing depths of the middle layer.

Figure 12a indicates that the maximum response at the ground will be for large gradients in the Scorer parameter between the lower and middle layer and the middle and upper layer with $h \sim 1.5$ km. Therefore, in order to investigate the mountain waves response to different l profiles, a high-response case initialized with $l_1 = 5l_2 = l_3/2$ and $h \sim 1.75$ km and a low-response case initialized with $l_1 = 5l_2 = l_3$ and $h \sim 1$ km are run. Inspection of Fig. 12b indicates that for the high-response case, the linear solution predicts $r = 0.82$. If we assume that the reflected and incident wave are exactly phase coherent, this reflection coefficient implies that the amplitude of the combined wave is $1 + \sqrt{r} = 1.9$. Since the momentum flux is given by $\rho u'w'$, and both u' and w' are enhanced by $\sqrt{r}$, the max-

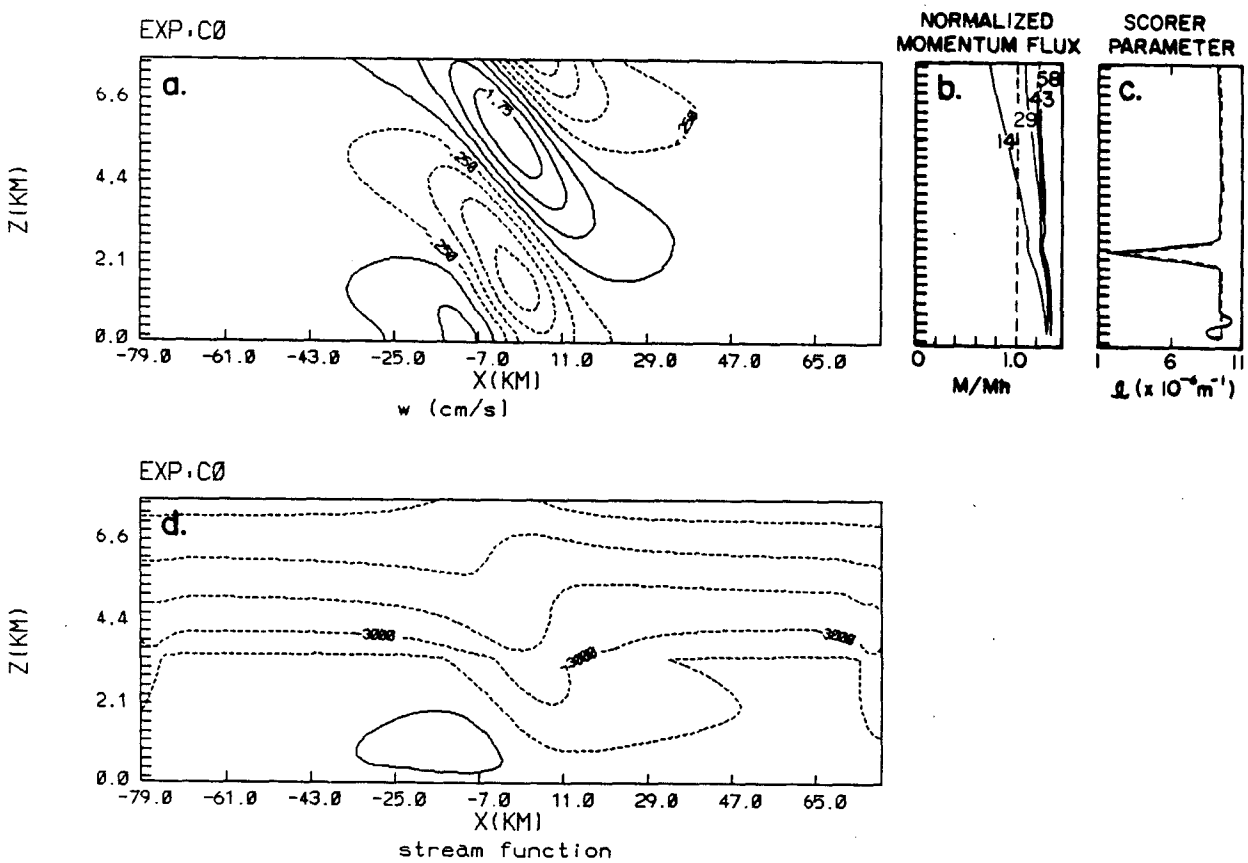

FIG. 13. Similar to Fig. 1 except for Expt. C0, which simulates flow over a 10 m mountain. Note that the model is initialized with the low-response stability profile indicated by the dotted Scorer parameter which is represented by "1" in Table 1 (see text for the descriptions of low- and high-response). The perturbation streamfunction is shown in panel (d) with contours of 2000 cm^2 s^{-1}.

imum surface stress predicted by linear theory should be 3.6. Because the mixed layer has zero thickness at the stability of $l_1/l_2 = 5$ in the low-response case (Fig. 14b), we can assume a slightly higher stability and an effective thickness of 250 m for the mixed layer and obtain a linearly predicted surface stress of 1.8. These two cases are run in four experiments with 10 m, 100 m, 500 m and 1000 m mountains. The graphs will be presented as before except that the perturbation streamfunction is also drawn for each case. The numbers after the experiment letter designate whether the experiment is initialized with a low-response (1) or a high-response (2) thermodynamic profile. The wind speed will be 10 m s^{-1} except in Expt. C0 where $U = 20$ m s^{-1}. The depth that the change in l takes place is ¼λ in this Expt. and all following experiments so that a maximum in the wave response is produced.

Experiment C0 (Fig. 13) indicates that when λ is large compared to the depth of the interface, there is not much reflection. Although there are slight divergences around the level where the Scorer parameter changes rapidly (Fig. 13c), the momentum flux reaches a nearly constant value with height.

When the vertical wavelength of the mountain wave is halved by halving the wind speed in experiment C1 (Fig. 14), the effect of the reflecting layer is pronounced. The surface momentum flux is almost 1.8 times the linear hydrostatic value. The high-response case (Expt. C2, Fig. 15) indicates that substantial reflection and positive interference between the incident and reflected wave has occurred. Surface momentum values 3.4 times larger than the hydrostatic value are produced. Only 30% of the wave energy escapes into the upper part of the model while three times this amount is present in Expt. C1. This indicates substantially more reflection from the interfaces. There is also little divergence in the momentum flux within the well-mixed layer.

When the mountain height is raised to 100 m (experimental group D), nonlinearities in the system begin to surface as evidenced by the oscillations in Figs. 16b and 17b. The nonlinearities are also seen by the modifications to the initial Scorer parameter. Since $Fr^{-1} = 0.19$, the strength of the nonlinearities are beginning to become significant.

In experimental group E, the mountain height is raised to 500 m producing strongly nonlinear flow. In E1 (Fig. 18), since $Fr^{-1} = 0.94$, wavebreaking is expected. The atmospheric profile, however, has inhibited the wavebreaking by reflecting enough energy to keep

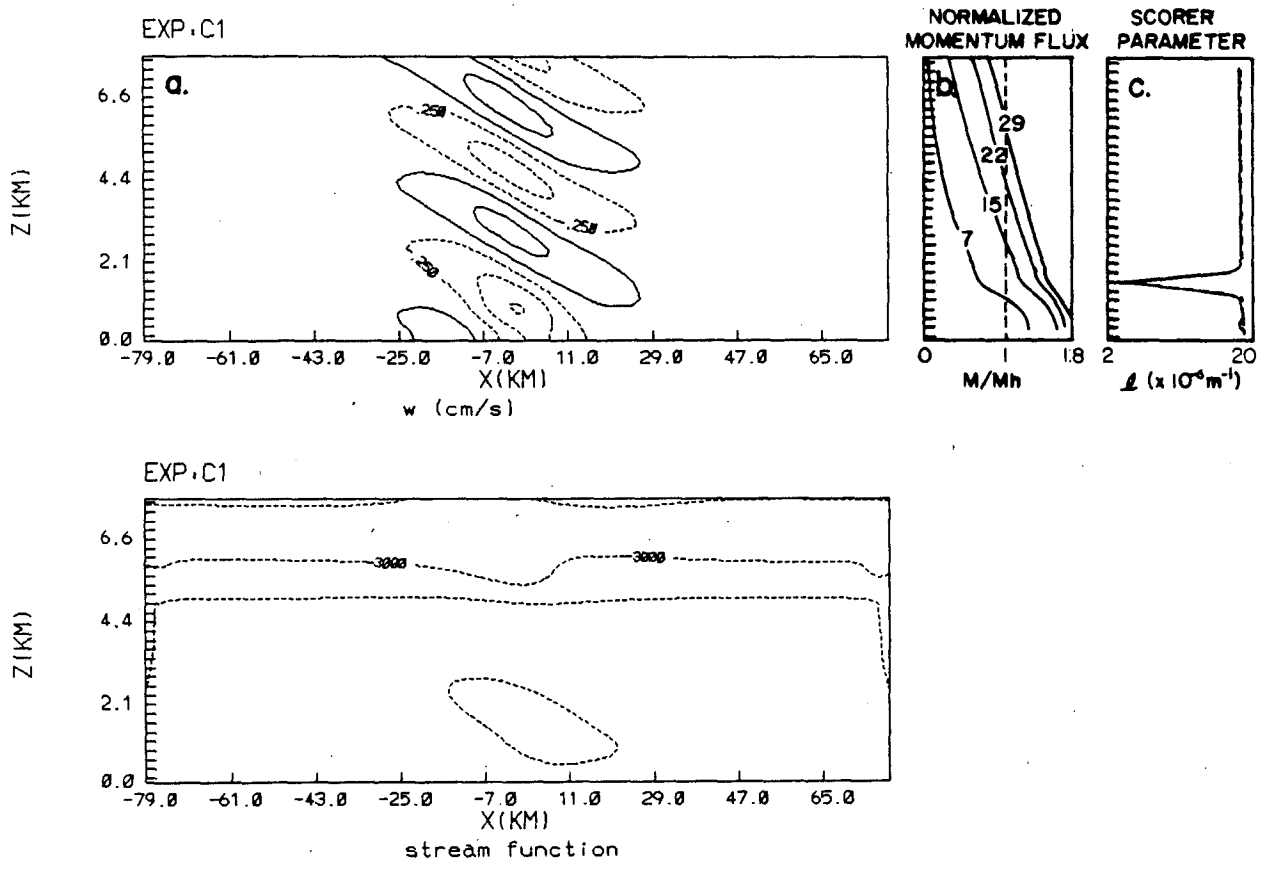

FIG. 14. Similar to Fig. 13 except for Expt. C1, which halves the zonal wind.

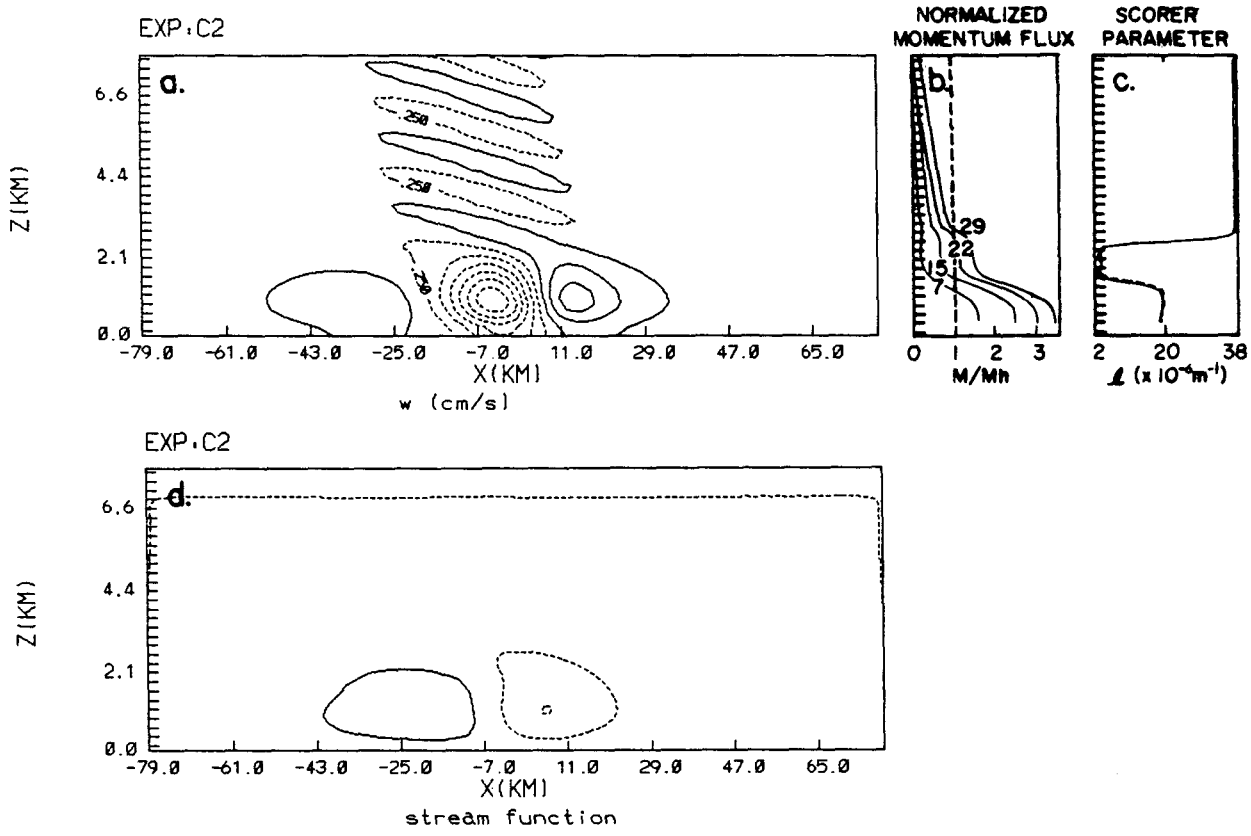

FIG. 15. Similar to Fig. 14 except for Expt. C2. Note that the model is initialized with the high-response stability profile indicated by the dotted Scorer parameter, which is represented by "2" in Table 1.

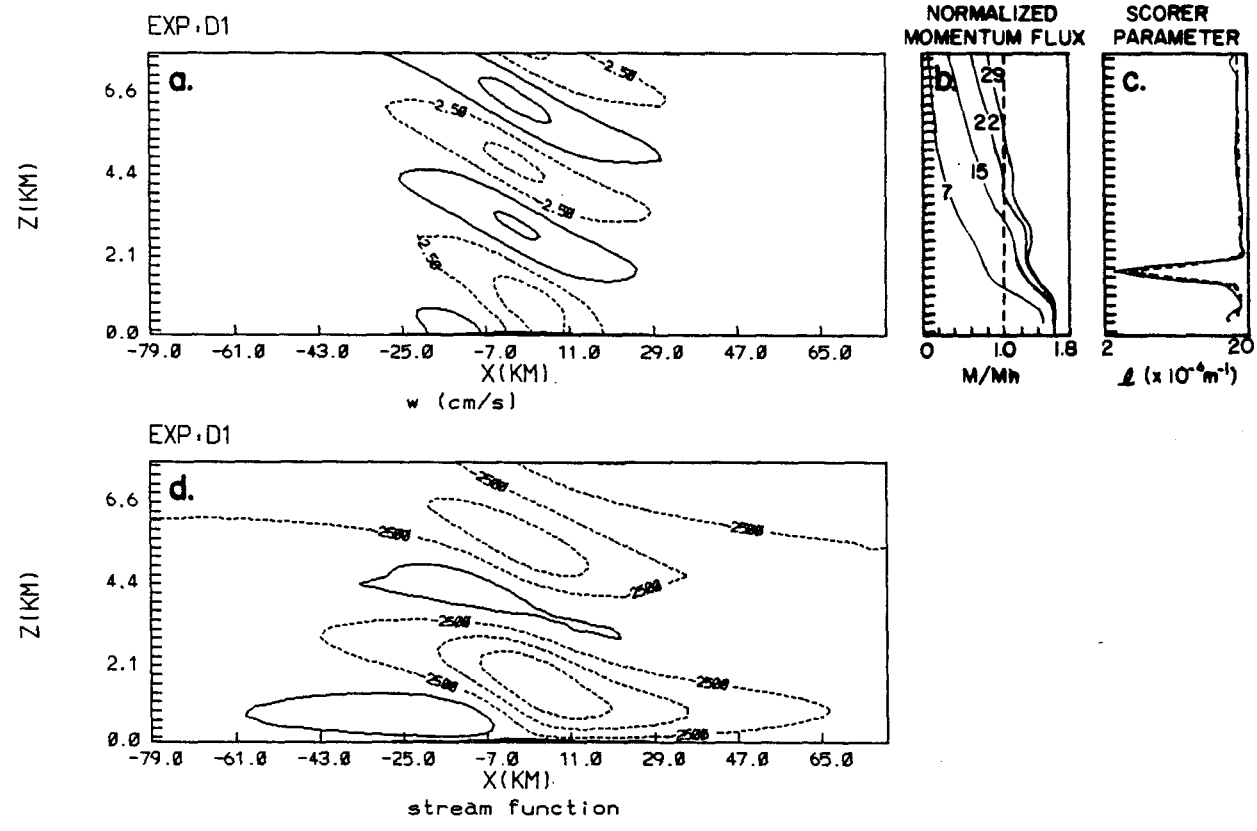

FIG. 16. Similar to Fig. 14 except for Expt. D1, which simulates flow over a 100 m mountain. Contours for the vertical motion and the perturbation streamfunction are 5 cm s^{-1} and 5000 cm^2 s^{-1}, respectively.

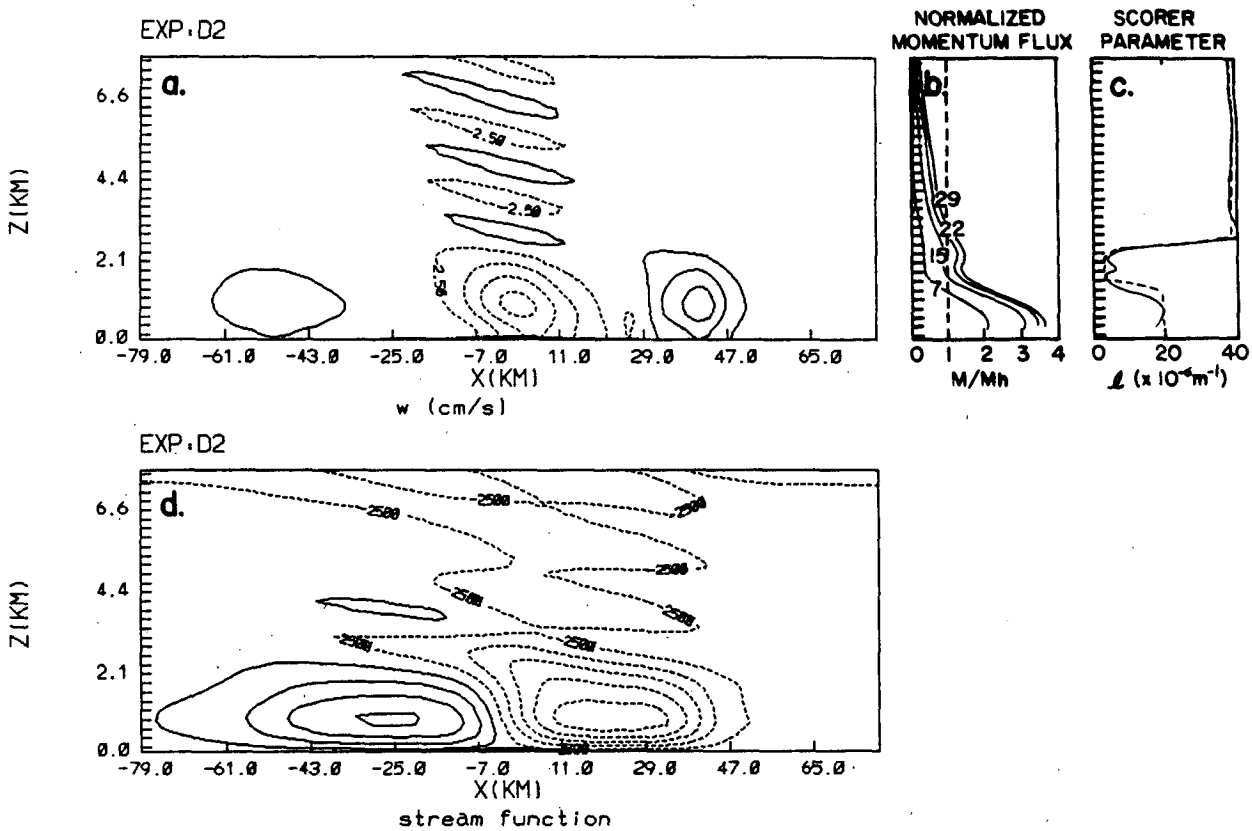

FIG. 17. Similar to Fig. 15 except for Expt. D2, which simulates flow over a 100 m mountain. Contours for the vertical motion and the perturbation streamfunction are 5 cm s^{-1} and 5000 cm^2 s^{-1}, respectively.

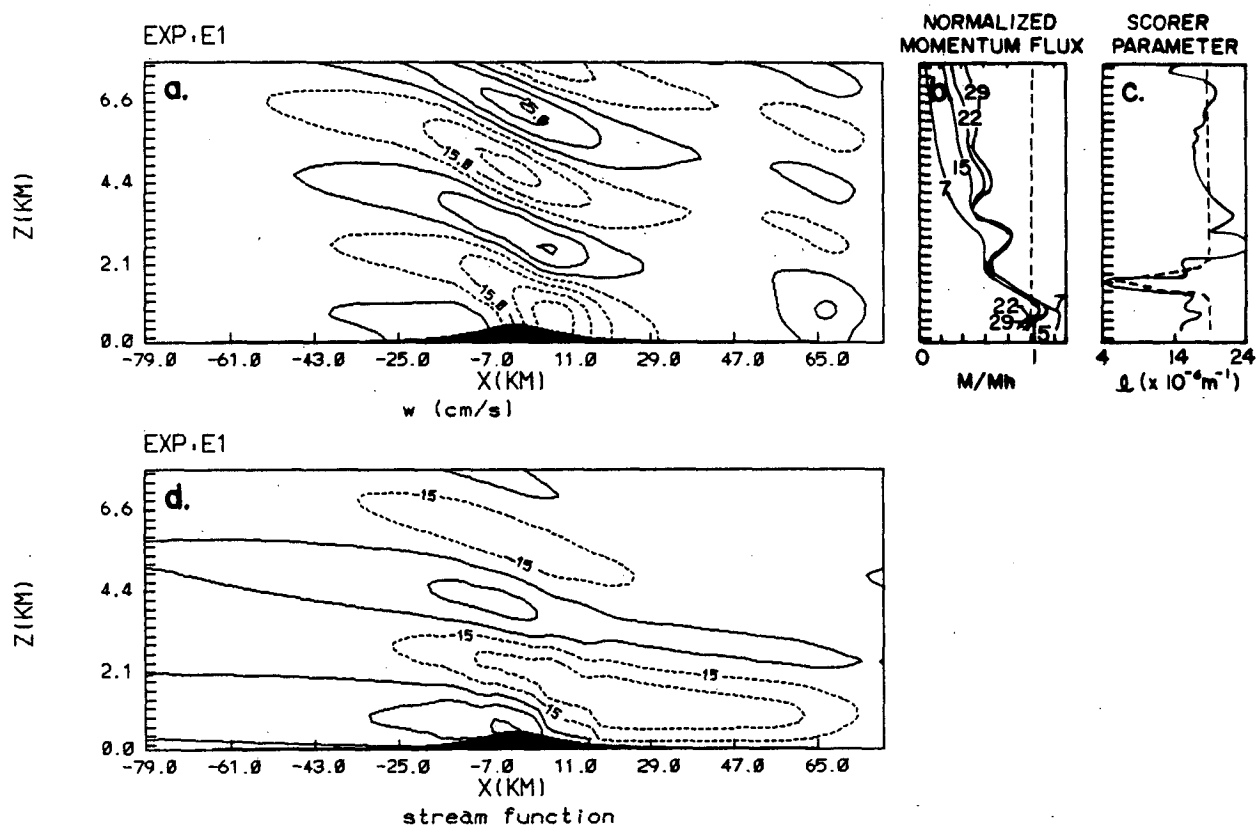

FIG. 18. Similar to Fig. 14 except for Expt. E1, which simulates flow over a 500 m mountain. Contours for the vertical motion and the perturbation streamfunction are 10 cm s^{-1} and 20 000 cm^2 s^{-1}, respectively.

the streamlines from overturning. The nonlinearity of the flow is seen by the strong oscillations in the momentum flux and also by the modifications to the initial Scorer parameter. In E2 (Fig. 19) the atmospheric profile allows the wavebreaking to occur as predicted.

In group F, the 1000 m mountain has produced wavebreaking with both low-response (Fig. 20) and high-response (Fig. 21) atmospheric profiles. It is interesting to note, however, that the level where the momentum flux reaches its analytic value is 500 m lower than when the atmospheric profile is undisturbed (compare Fig. 20b and Fig. 4b). This indicates that the ambient conditions can influence the level where wavebreaking occurs.

An interesting feature of these nonlinear experiments can be seen in the motion of the low-level vertical motion patterns. Comparing the high-response cases (Figs. 15a, 17a and 19a) the upward vertical motion centers move away from the mountain with time, similar to the movement observed in the simulations by Lilly and Klemp (1979). As the mountain height increases, the vertical motion centers are located further from the center of the domain. The perturbation streamfunctions (Figs. 15d, 17d and 19d) point to the existence of a vortex couplet which separates with time as each vortex propagate in opposite directions. As the mountain height rises and Fr^{-1} increases, these couplets are stronger and move faster. These couplets are strongest in the high-response cases because the low-level flow is decoupled from the upper flow by the mixed layer, allowing the vortex couplets to evolve pseudoindependently of the mean flow. Although this pattern can be seen in the low-response cases (as in Fig. 18), it is significantly reduced by the exchange of momentum between the blocked flow and the flow aloft.

The results for these experiments are summarized in Fig. 22 where the magnitude of the surface momentum flux is plotted against the inverse Froude number. Where needed, additional data have been supplied by additional numerical model runs. The dotted line indicates the response of nonlinearities in a single layer atmosphere taken from Durran (1986). The response increases slightly with increasing mountain height until the wave breaks at $Fr^{-1} = 0.75$. Note the efficient trapping of wave energy below the reflecting layer. Durran (1986) points out that the decreased threshold for wavebreaking is due to the decrease in density with height in the atmosphere.

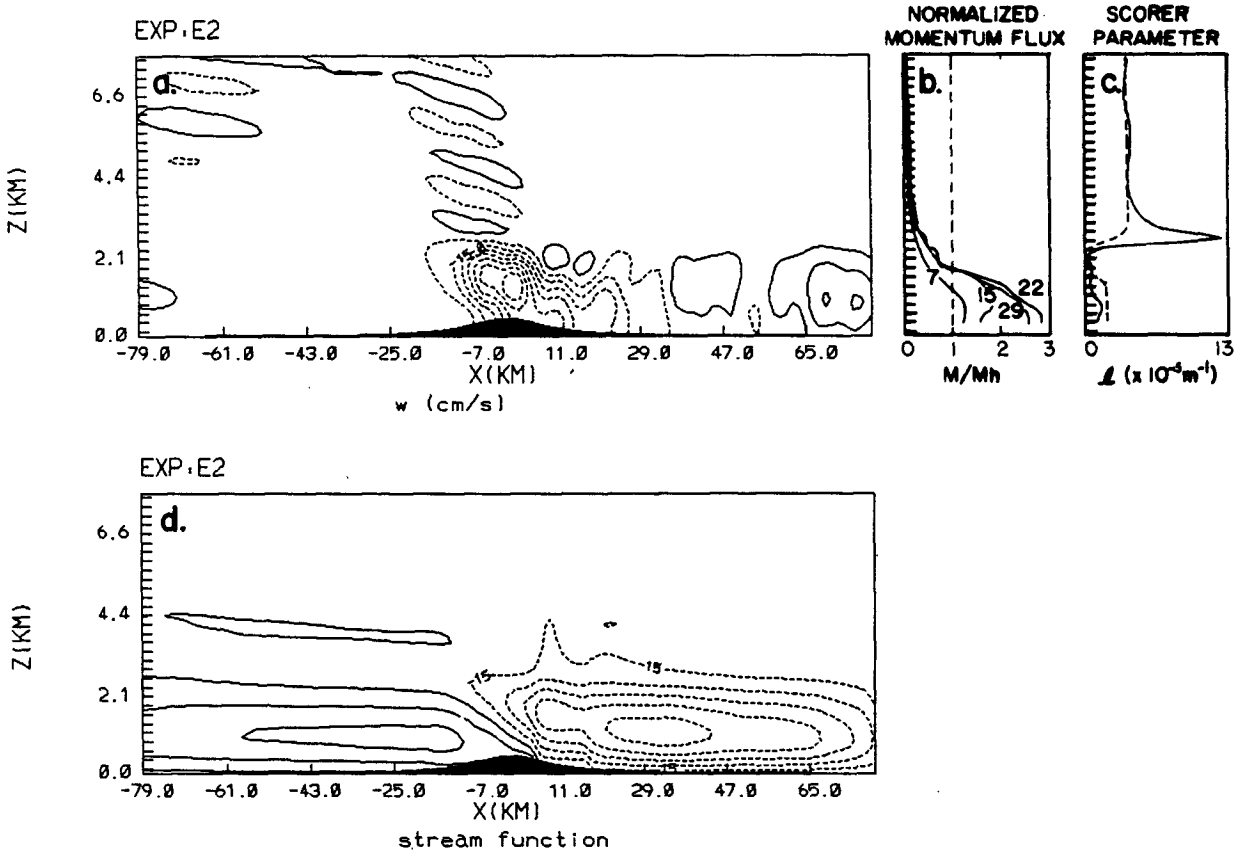

FIG. 19. Similar to Fig. 15 except for Expt. E2, which simulates flow over a 500 m mountain. Contours for the vertical motion and the perturbation streamfunction are 10 cm s^{-1} and 20 000 cm^2 s^{-1}, respectively.

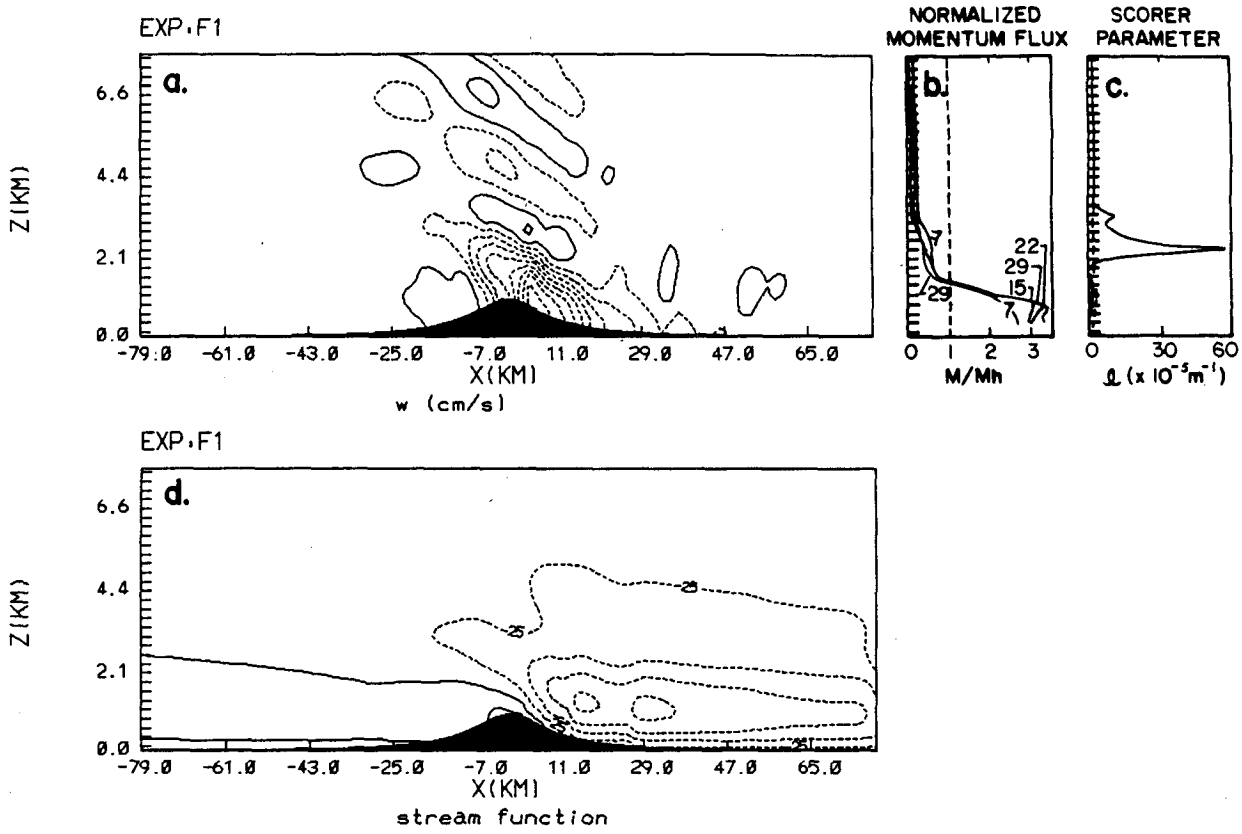

FIG. 20. Similar to Fig. 14 except for Expt. F1, which simulates flow over a 1000 m mountain. Contours for the vertical motion and the perturbation streamfunction are 20 cm s^{-1} and 50 000 cm^2 s^{-1}, respectively.

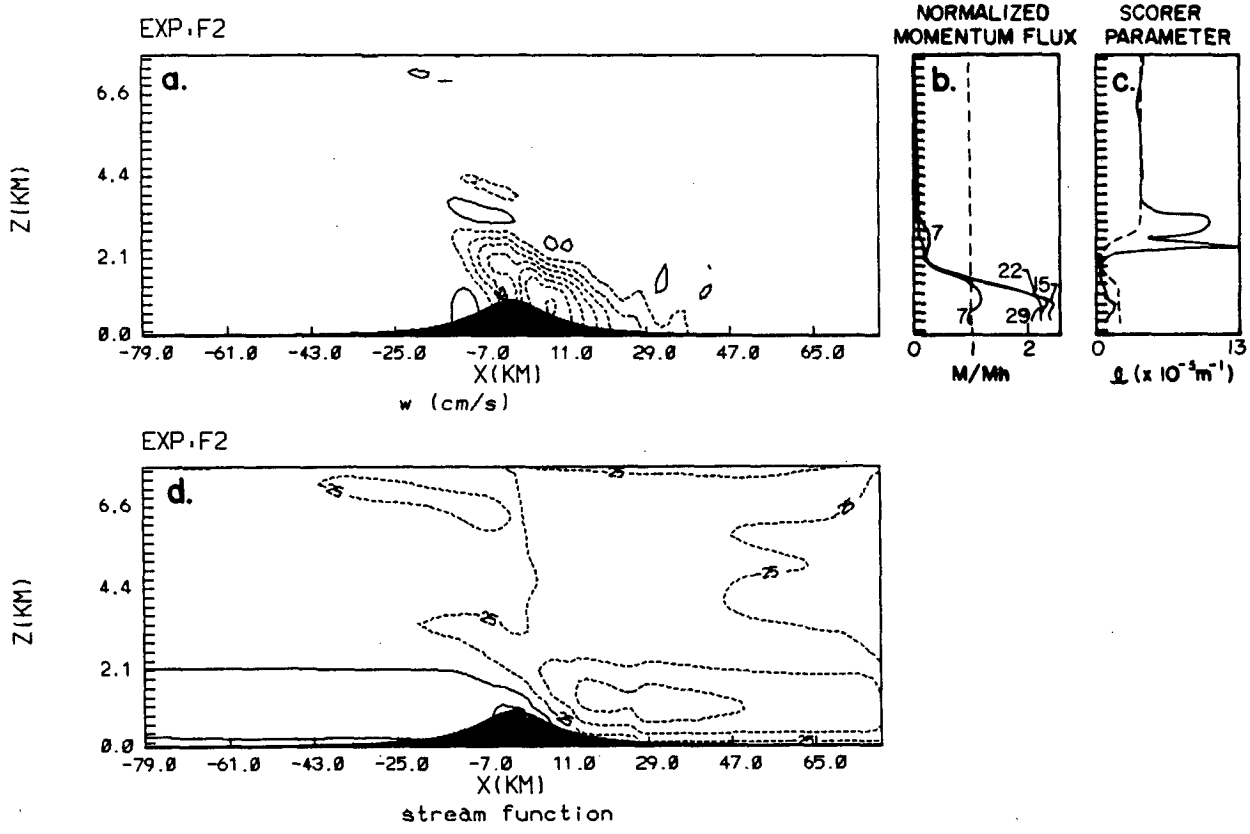

FIG. 21. Similar to Fig. 15 except for Expt. F2, which simulates flow over a 1000 m mountain. Contours for the vertical motion and the perturbation streamfunction are 20 cm s^{-1} and 50 000 cm^2 s^{-1}, respectively.

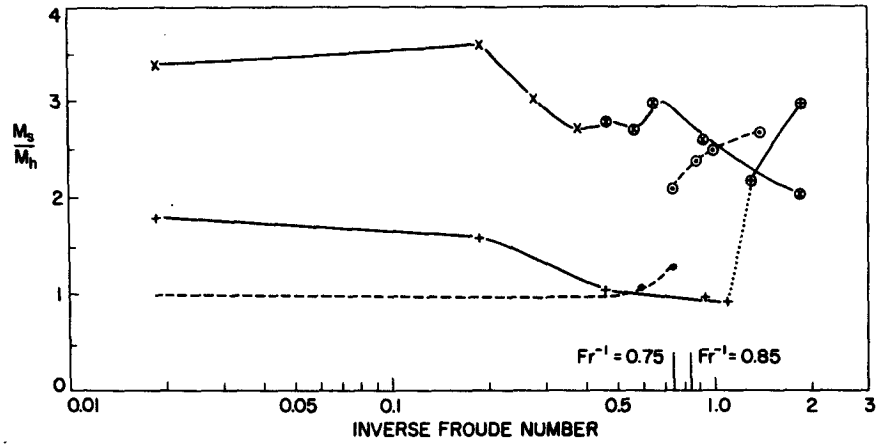

FIG. 22. A log-linear plot of surface momentum flux as a function of the inverse Froude number. The ●'s represent the solutions found by Durran (1986) for a one-layer atmosphere, +'s represent solutions for the low-response case and x's represent solutions for the high-response case (see text for the descriptions of low- and high-response). Circled markers indicate that wavebreaking has occurred in the solutions. The transition between a wavebreaking state and a nonwavebreaking state occurs abruptly within the Froude numbers indicated by the dotted line in the low-response case, at $Fr^{-1} = 0.75$ in Durran's simulations and is not abrupt in the high-response case.

The low-response case is delineated by the lower solid line. In contrast to Durran (1986), the nonlinearities of the system decrease the surface momentum flux as the mountain height increases. This is probably due to the multiple reflection layers which become more important as the mountain height increases. Figure 18b shows the multiple layers from which wave reflection may occur. As the nonlinearities in the system become stronger, the multiple reflections become stronger as these layers become thicker and the transitions between them become more abrupt. Finally, at $Fr^{-1} \sim 1.2$, the wave breaks and the wave response precipitously increases. The greatly increased threshold for wavebreaking is due to the increased reflection and thus decreased transmission of energy to the wavebreaking height.

The upper solid line delineates the high-response case. As the mountain height increases, the system response increases until $Fr^{-1} \sim 0.2$. At this point the surface momentum flux decreases until wavebreaking occurs. The increase in wave response for $Fr^{-1} < 0.2$ is similar to the increase in wave response Durran simulated and is occurring because the deep mixed layer is effectively trapping wave energy and suppressing the multiple reflection levels from developing. At $Fr^{-1} > 0.2$, enough of the wave energy escapes to modify the flow aloft and produce the disruptive multiple reflections. Wavebreaking occurs at the threshold $Fr^{-1} \sim 0.5$ due to the large accumulation of wave energy in the lowest layer. The wave will break at quite lower mountain heights in the high-response case than for the low-response case and both thresholds are significantly different from the threshold predicted by linear theory. It is interesting to note that the transition to the wavebreaking regime in the high-response case is smooth, probably because there is not much difference between the magnitudes of the two solutions. The linear analytic solutions appear to be within ~10% of the nonlinear solutions for $Fr^{-1} < 0.2$. The laminar wave response for the three-layer atmosphere is also greater than any wavebreaking response simulated in these nonlinear experiments.

5. Conclusions

We have shown that moisture, radiation and nonlinear effects influence the propagation of the mountain wave and modify the corresponding momentum flux profile. The reduction of the momentum flux due to moisture is determined by the ratios of the moist to dry Brunt–Väisäla frequencies. This is to be expected; however, by reducing the wave's momentum flux, moisture can inhibit the onset of wavebreaking. Longwave radiational cooling can significantly alter the ambient environmental stability profile and allow conditional instability to develop. The resulting convection disrupts and in some cases eliminates the propagation of mountain wave energy through the cloud layer. This has strong implications for GCMs since unresolved wave stress divergences are hypothesized to play an important role in the westerly momentum budget, especially in the Northern Hemisphere winters. While the wavebreaking scheme proposed by Palmer et al. (1986) does appear to alleviate the systematic biases in the PBL and stratosphere, we feel that the radiational destabilization near the tops of clouds might require a more judicious use of the wave breaking scheme.

We have dealt primarily with low level clouds since

we wanted to isolate moisture and radiational influences from wavebreaking effects. Because wavebreaking appears to be an efficient reflector of wave energy, clouds which appear above the wavebreaking level would presumably have little impact on the vertical wave stress profile. If the breaking level is above the high level clouds, then certainly these clouds will also affect the propagation of the mountain wave. Since high clouds may radiationally heat or cool, however, the precise effect of high clouds on mountain wave propagation remains unclear.

Chen and Cotton (1987) and others have shown that the magnitude of radiational cooling is dependent on the gradient of moisture at cloud top and the moisture profile aloft. A moist unsaturated atmosphere above cloud top or the presence of high level clouds can substantially decrease the radiative cooling of the low level clouds, producing an environment which may allow the mountain waves to propagate through the low level clouds relatively unhindered. Including cloud effects on wave drag in a GCM will be quite a challenge, then, since both the discontinuous liquid water distribution through the cloud and the water vapor content of the overlaying air mass must be accurately predicted or diagnosed to infer the correct radiationally modified temperature profile.

The height and thickness of the relative minimum in the Scorer parameter in relation to the dominant vertical wavelength of the mountain wave is important in determining the magnitude of the wave stress divergence in the low levels. Largest wave stress divergences occur with thick layers (to promote strong reflection of the incident wave) which are an odd integral multiple of $\frac{1}{4}\lambda$ above the ground (to promote positive interference).

The nonlinearities of orographic mountain waves create subtle changes in the expected linear response. The nonlinearities of the system tend to decrease the wave response at the ground due to the development of multiple reflecting layers caused by the wave interacting with the mean flow. If the lower layer can be efficiently decoupled from the flow aloft, however, nonlinearities can reinforce the linear wave response. The onset of wavebreaking may be significantly delayed and the height at which the wave breaks may be significantly altered by the ambient thermodynamic profile.

Acknowledgments. We would like to thank Dr. Gregory Tripoli for his technical assistance in running the CSU RAMS and Dr. David Randall and Jerome Schmidt for helpful discussions. Thanks also to Brenda Thompson for help in preparing this manuscript and Lucy McCall for drafting the figures. This research was funded in part by the National Science Foundation under grant ATM-8512480 and the Army Research Office under contract DAAL03-86-K-0175. All computations were performed on the National Center for Atmospheric Research (NCAR) Cray X-MP48 computer. NCAR is supported by the National Science Foundation.

REFERENCES

Blumen, W., 1965: A random model of momentum flux by mountain waves. *Geofys. Publ.*, **26**, 1–33.

Chen, C., and W. R. Cotton, 1983: A one-dimensional simulation of the stratocumulus-capped mixed layer. *Bound. Layer Meteor.* **25**, 289–321.

——, and ——, 1987: The physics of the marine stratocumulus-capped mixed layer. *J. Atmos. Sci.*, **44**, 2951–2977.

Clark, T. L., and W. R. Peltier, 1984: Critical level reflection and the resonant growth of nonlinear mountain waves. *J. Atmos. Sci.*, **41**, 3122–3134.

Durran, D. R., 1986: Another look at downslope windstorms. Part I: The development of analogs to supercritical flow in an infinitely deep continuously stratified fluid. *J. Atmos. Sci.*, **43**, 2527–2543.

——, and J. B. Klemp, 1982: On the effect of moisture on the Brunt–Väisäla frequency. *J. Atmos. Sci.*, **39**, 2152–2158.

——, and ——, 1983: A compressible model for the simulation of moist mountain waves. *Mon. Wea. Rev.*, **111**, 2341–2361.

Eliassen, A., and E. Palm, 1961: On the transfer of energy in stationary mountain waves. *Geofys. Publ.*, **22**, 1–23.

Emanuel, K. A., 1986: Overview and definition of mesoscale meteorology. *Mesoscale Meteorology and Forecasting*, P. S. Ray, Ed., Amer. Meteor. Soc., 1–17.

Klemp, J. B., and D. K. Lilly, 1975: The dynamics of wave-induced downslope winds. *J. Atmos. Sci.*, **32**, 320–339.

——, and D. R. Durran, 1983: An upper boundary condition permitting internal gravity wave radiation in numerical mesoscale models. *Mon. Wea. Rev.*, **111**, 430–444.

Lilly, D. K., and J. B. Klemp, 1979: The effects of terrain shape on nonlinear hydrostatic mountain waves. *J. Fluid. Mech.*, **95**, 241–261.

Palmer, T. N., G. J. Shutts and R. Swinbank, 1986: Alleviation of a systematic westerly bias in general circulation and numerical weather prediction models through an orographic gravity wave parameterization. *Quart. J. Roy. Meteor. Soc.*, **112**, 1001–1039.

Rind, D., R. Suozzo, N. K. Balachandran, A. Lacis and G. Russell, 1988. The GISS global climate-middle atmosphere model. Part I: Model structure and climatology. *J. Atmos. Sci.*, **45**, 329–370.

Scorer, R. S., 1949: Theory of waves in the lee of mountains. *Quart. J. Roy. Meteor. Soc.*, **75**, 41–56.

Slingo, A., and D. W. Pearson, 1987: A comparison of the impact of an envelope orography and of a parameterization of orographic gravity-wave drag on model simulations. *Quart. J. Roy. Meteor. Soc.*, **113**, 847–870.

Smith, R. B., 1979: The influence of mountains on the atmosphere. *Advances in Geophysics*, Vol. 21, Academic Press, 87–230.

Tripoli, G. J., and W. R. Cotton, 1982: The Colorado State University three-dimensional cloud/mesoscale model—1982. Part I: General theoretical framework and sensitivity experiments. *J. Rech. Atmos.*, **16**, 185–219.

——, and ——, 1989a: A numerical study of an observed orogenic mesoscale convective system. Part I: Simulated genesis and comparison with observations. *Mon. Wea. Rev.*, **117**, 273–304.

——, and ——, 1989b: A numerical study of an observed orogenic mesoscale convective system. Part II: Analysis of governing dynamics. *Mon. Wea. Rev.*, **117**, 305–328.

Wallace, J. M., S. Tibaldi and A. J. Simmons, 1983: Reduction of systematic errors in the ECMWF model through the introduction of an envelope orography. *Quart. J. Roy. Meteor. Soc.*, **109**, 683–718.

Wesley, D. A., and R. A. Pielke, 1989: Observations of blocking-induced convergence zones and effects on precipitation in complex terrain. *Atmos. Res.*, (in press).